ARCHIVES OF MECHANICS
Arch. Mech. **77** (3), 263–287, 2025, https://doi.org/10.24423/aom.4642

A simple quasi-3D theory for static stability analysis of imperfect FG beam

A. MENASRIA[1,5*)], R. SLIMANI[2)], A. BOUHADRA[1,5)], S. REFRAFI[1)], M. CHITOUR[3)], M. ALI RACHEDI[1)], N. HIMEUR[3)], K. ZERARI[4)]

[1)] *University of Khenchela, Faculty of Sciences and Technology, Civil Engineering Department, BP 1252 Road of Batna, Khenchela 40000, Algeria,*
[*)] *e-mail: abderrahmane.menasria.24@gmail.com (corresponding author)*

[2)] *University of Tamanghasset, Faculty of Sciences & Technology, Sciences & Technology Department, BP 10034, Sersouf Tamanghasset 11000, Algeria*

[3)] *University of Khenchela, Faculty of Sciences and Technology, Mechanic Engineering Department, BP 1252 Road of Batna, Khenchela 40000, Algeria*

[4)] *University Center of Mila, Institute of Science and Technology, Mechanical and Electromechanical Engineering Department, BP No 26 RP Mila 43000 Algeria*

[5)] *Materials and Hydrology Laboratory, University of Sidi Bel Abbes, Faculty of Technology, Civil Engineering Department, BP 89, Sidi Bel Abbes 22000, Algeria*

This study introduces a simplified approach to assess the buckling and static bending of advanced composite beams, including those composed of functionally graded materials (FGMs) with various porosity models. The technique utilizes a straightforward integral quasi-3D approach based on the advanced shear deformation theory. This approach offers several advantages: it simplifies the analysis by reducing the number of unknowns and equations required, improves accuracy by considering the stretch effect across the entire depth of the beam, resulting in more reliable results, and accurately represents shear by satisfying the zero-traction boundary conditions on the beam's surfaces without the need for a shear correction factor. Additionally, it captures the parabolic pattern of transverse shear strain and stress throughout the depth of the beam. The governing equations are obtained by applying the concept of virtual work, and the Navier solution is employed to calculate analytical solutions for the buckling and static bending of FGM porous beams under different boundary conditions. The approach is in line with and builds upon existing research on FGMs and other sophisticated composite beams, further enhancing its validity and reliability. Finally, computational analyses demonstrate how the distribution of materials, such as power-law functionally graded materials (FGMs), geometry, and porosity, affect the deflections, stresses, and critical buckling load of the beam.

Key words: higher-order shear deformation theory, FG beam, integral quasi-3D, bending, buckling, porosity, virtual work principle, Navier solution.

1. Introduction

Functionally graded materials (FGMs) have been an engineering topic for around 30 years since their concept was first proposed in 1987. The scientific and engineering community working on FGM has become an important and continually growing part of the materials science and engineering community. FGMs are found in innumerable structures, systems, tools, and objects today, from microelectromechanical (MEMS) and other microstructures to space shuttles because they contribute to making these objects cheaper, safer, more efficient, and sometimes simply feasible. In recognition of their importance, they have become regulated by many standards set by engineering and scientific associations [1, 2].

The unique properties of FGMs have attracted significant research interest in their bending behaviour under various loading conditions. This includes static bending, free vibration analysis, and buckling behaviour of FGM beams, plates, and shells [3]. Literature suggests that the FGM plate analysis can be approached through various theoretical frameworks, including the classical plate theory (CPT) [4, 5]. The first-order shear deformation theory (FSDT) [6, 7], the higher-order shear deformation theory [8–10], the quasi-3D theory and the Carrera Unified Formulation (CUF) [11, 12]. To determine the spatial variation of material properties in functionally graded materials and structures, mathematical laws such as the exponential law [13], sigmoid law [14], and power law [15] are used.

According to the literature, some work using a higher shear deformation plate theory (HSDT) with integral terms to determine the behaviour of plates in FGM has been published. Menasria *et al.* [16] investigate the free vibration behaviour of functionally graded sandwich plates (FGSPs) with a ceramic foam core supported by a viscoelastic foundation. The study specifically examines the impact of temperature variations on the vibration characteristics of these structures. The analysis incorporates the effects of damping and explores various configurations of FGSPs. A quasi-3D theory is employed to reduce the number of displacement variables and simplify the governing equations through the use of integral terms. Two models are considered to account for the non-uniform properties of the ceramic foam core. Himeur *et al.* [17] examined the bending behaviour of functionally graded (FG) plates under various loading conditions using a novel quasi-3D theory. The theory incorporates the combined influence of non-uniform Winkler–Pasternak foundations, where two foundation parameters change simultaneously across the plate's surface. This approach builds upon existing quasi-3D theories by explicitly considering the coupling effect between the variable foundation and the diverse loading scenarios acting on the FG plates. Many studies have been conducted recently on FG beams. Belarbi *et al.* [18] conducted a study on the flexural analysis of Ti-6Al-4V/ZrO2 functionally graded sandwich plates

subjected to combined thermal and mechanical loading, utilising an exponential-cubic-sinusoidal integral shear deformation theory. The proposed formulation offers a parabolic distribution of transverse shear stresses, eliminating the need for additional factors in the model. The analysis considers various sandwich plate configurations with different layer thicknesses and material types, where the FG layers exhibit a continuous and smooth variation based on exponential and power-law functions. Berkia *et al.* [19] investigated the mechanical buckling behaviour of bi-directional functionally graded sandwich beams (BFGSW) under various boundary conditions using a quasi-3D beam theory that incorporates an integral term within the displacement field. However, the covering layers of the beams vary smoothly along the beam length and thickness directions. Houri *et al.* [20] investigated the wave dispersion behaviour in porous FG carbon nanotube-reinforced composite (CNTRC) beams. These beams consist of four different patterns of single-walled carbon nanotubes (SWCNTs) distributed within a polymer matrix. The material properties of the CNTRC beams are estimated using a mixture rule. A novel aspect of this study is the introduction of three porosity models that describe the porosity distributions within the matrix. Additionally, a three-unknown integral higher-order shear deformation theory (HSDT) is employed to analytically model the CNTRC beams, incorporating a new shape function that characterises the distributions of shear stresses and strains.

Various publications have explored the effect of porosity on the behaviour of FGM beams, including Ghazwani *et al.* [21] studied the nonlinear forced vibrations of sandwich beams made from porous FGMs with a viscoelastic core layer; their analysis employs higher-order Zig-Zag theories to account for both normal and shear deformations. Slimani *et al.* [22] developed a quasi-three-dimensional (3D) refined theory based on a novel higher-order shear deformation approach to analyse the static bending behaviour of advanced composite plates, such as functionally graded plates, with two distinct types of porosity distribution. This approach reduces the number of unknowns and governing equations by incorporating the effect of thickness stretching into the transverse displacement, bending, and shear, using a newly defined shape function. Tamrabet *et al.* [23] studied the impact of porosity on the buckling behaviour of a thick functionally graded sandwich plate subjected to various boundary conditions and in-plane loads. The formulation is based on a newly developed sandwich plate structure, utilising a FGM characterised by a modified power law function with both symmetric and asymmetric configurations. Four distinct porosity distributions are examined, and their variations are aligned with the material property gradient across the thickness of the face sheets. Additionally, the study considers a second model of the sandwich plate, which incorporates a metal foam core with functionally graded material face sheets.

This study aims to create a novel 2D and quasi-3D HSDT shear deformation theory incorporating integral terms. This theory is used to analyse the static bending and buckling characteristics of beams made of FGM with porosities. Furthermore, the study takes into account the impact of stretching. The novelty of this research lies in using a quasi-3D HSDT theory that accounts for the effect of transverse stretching, which is generally not considered in conventional 2D shear deformation theories. This approach reduces the number of variables to three, unlike other similar theories that often involve four or more variables, thus simplifying the problem by incorporating a simple integral HSDT. Additionally, a displacement field with a coefficient n is introduced. This coefficient facilitates the transition from 2D to quasi-3D theories without any discontinuity and allows for a more detailed examination of the equilibrium and stability of FG beams. The suggested beam is equipped with four different types of porous distribution. It is subjected to static bending and buckling tests, with various boundary conditions being considered. The beam is believed to possess consistent material qualities (isotropic) at every specific point. The Young modulus of the beam varies across its thickness in accordance with a power law that depends on the volume fractions of the materials present. This theory imposes equilibrium conditions on the upper and lower surfaces of the beam, eliminating the need for shear correction components. To examine the beam's behaviour, the governing equations are obtained by applying the principle of virtual work and subsequently solved using the Navier method. To ascertain the precision and efficacy of this novel theory, the computed outcomes are juxtaposed with those derived from existing well-established theories. In addition, the study presents and discusses an extensive range of parametric studies to investigate the impact of different factors on the behaviour of the system.

2. Material properties of imperfect FGM beams

The FG beam's varied boundary conditions of length (l) and thickness (h) are exposed, where the material composition varies along the z direction with the FG index k (Fig. 1). The mechanical properties of the FG beam, such as Young's modulus E, Poisson's ratio υ, and shear modulus G, change as the material composition changes.

In this study, FGM beams with the power-law function (P-FGM), the volume of ceramic is obtained using the following formula:

$$V(z) = \left(\frac{1}{2} + \frac{z}{h}\right)^k. \tag{2.1}$$

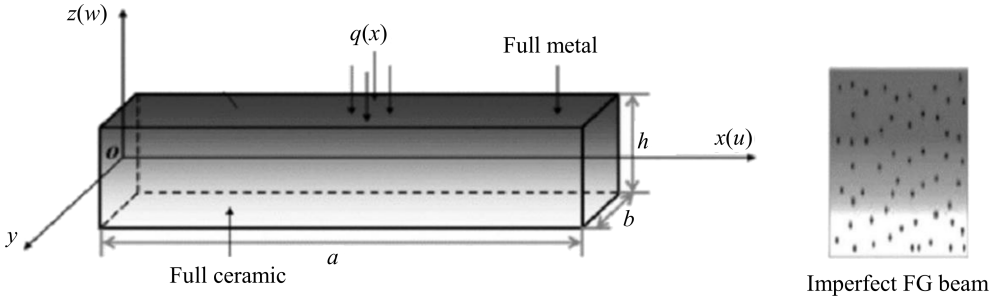

Fig. 1. Geometry and coordinate system of the imperfect FG beam.

In this case, k is the power-law index, and h is the thickness of the beam. The material properties of a P-FGM can be determined as:

$$P(z) = P_2 + (P_1 - P_2)V(z). \tag{2.2}$$

The porosity effect is investigated. Researchers have proposed numerous models of porosity distribution to compute the effective material properties of porous FGM beams; four porosity models are used (Fig. 1) by Patil *et al.* [24].

Porous material properties for various porosity patterns and the porosity coefficient (Ω) are given by:

Imperfect I:

$$P(z) = (P_c - P_m)V_c + P_m - \frac{\Omega}{2}(P_c + P_m), \tag{2.3a}$$

Imperfect II:

$$P(z) = (P_c - P_m)V_c + P_m - \frac{\Omega}{2}(P_c + P_m)\left(1 - \frac{2|z|}{h}\right), \tag{2.3b}$$

Imperfect III:

$$P(z) = (P_c - P_m)V_c + P_m - \frac{\Omega}{2}(P_c + P_m)\left(\frac{1}{2} + \frac{z}{h}\right), \tag{2.3c}$$

Imperfect IV:

$$P(z) = (P_c - P_m)V_c + P_m - \frac{\Omega}{2}(P_c + P_m)\left(\frac{2|z|}{h}\right). \tag{2.3d}$$

3. Theoretical formulations of the FG beam

3.1. Kinematics and strains

A new reformulation has been developed to give the displacement field of the conventional HSDT:

$$u(x,z) = u_0(x) - z\frac{\partial w_0}{\partial x} + f(z)\varphi_x(x), \qquad w(x,z) = w_0(x) + ng(z)\theta(x), \tag{3.1}$$

u_0, w_0, θ, φ_x are the four unknown displacements of the mid-plane of the beam. By considering that $\varphi_x = \int \theta\,(x)\,dx$ and taking into account the stretching effect:

$$u(x,z) = u_0(x) - z\frac{\partial w_0}{\partial x} + k_a f(z)\int \theta(x)\,dx, \qquad w(x,z) = w_0(x) + n\,g(z)\theta(x). \tag{3.2}$$

The integrals used in the above equations shall be resolved by a Navier-type method and can be given as follows:

$$\int \theta\,dx = A'\frac{\partial\theta}{\partial x}, \tag{3.3}$$

where the coefficients A' is expressed according to the type of solution used, in this case, via Navier. Therefore, A' and k_a are expressed as follows:

$$A' = -\frac{1}{\alpha^2}, \quad k_a = -\alpha^2 \quad \text{and} \quad \alpha = \frac{m\pi}{a}, \tag{3.4}$$

$f(z)$ represents the shape function defining the distribution of transverse shear deformation; it is represented as [25]:

$$f(z) = z\left(1 - \frac{4}{3}\frac{z^2}{h^2}\right) \quad \text{and} \quad g(z) = \frac{2}{15}\frac{df(z)}{dz}, \tag{3.5}$$

n is a real number and is given as follows:

$$n = \begin{cases} 0 & \text{for } 2D, \\ 1 & \text{for quasi-3D.} \end{cases} \tag{3.6}$$

Based on the elasticity theory, the non-zero linear strain components obtained from Eqs. (3.5) and (3.6) are:

$$\varepsilon_x = \varepsilon_x^0 + zk_x^b + f(z)k_x^s, \ \{\gamma_{xz}\} = f'(z)\{\gamma_{xz}^0\} + g(z)\{\gamma_{xz}^1\}, \ \varepsilon_z = g'(z)\varepsilon_z^0, \tag{3.7a}$$

where

$$\{\varepsilon_x^0\} = \left\{\frac{\partial u_0}{\partial x}\right\}, \qquad \begin{Bmatrix} k_x^b \\ k_x^s \end{Bmatrix} = \begin{Bmatrix} -\dfrac{\partial^2 w_0}{\partial x^2} \\ k_1\theta \end{Bmatrix},$$
$$\{\gamma_{xz}^0\} = \left\{k_1\int \theta\,dx\right\}, \quad \{\gamma_{xz}^1\} = \left\{\frac{\partial\theta}{\partial x}\right\}, \tag{3.7b}$$
$$\varepsilon_z^0 = \theta.$$

Assuming that the perfect and imperfect FG beam material follows Hook's law, the linear elastic constitutive equations at a point are:

$$\begin{Bmatrix} \sigma_x \\ \sigma_z \\ \tau_{xz} \end{Bmatrix} = \begin{bmatrix} C_{11} & C_{13} & 0 \\ C_{13} & C_{33} & 0 \\ 0 & 0 & C_{55} \end{bmatrix} \begin{Bmatrix} \varepsilon_x \\ \varepsilon_z \\ \gamma_{xz} \end{Bmatrix}. \tag{3.8}$$

The C_{ij} $(i, j = 1, 3, 5)$ expressions in terms of engineering constants depending on the normal strain ε_z, are given below

• Case of 2D ($\varepsilon_z = 0$), then C_{ij} are:

$$C_{ij} = E \quad (i = 1); \qquad C_{ii} = \frac{E(z)}{2(1+\nu(z))} \quad (i = 5). \tag{3.9a}$$

• Case of quasi-3D ($\varepsilon_z \neq 0$), then C_{ij} are:

$$\begin{aligned} C_{ii} &= \frac{E(z)}{1-\nu^2(z)} \qquad (i = 1, 3), \\ C_{ij} &= \frac{E(z)\nu(z)}{1-\nu^2(z)} \qquad (i, j = 1, 3), \\ C_{ii} &= \frac{E(z)}{2(1+\nu(z))} \quad (i = 5). \end{aligned} \tag{3.9b}$$

3.2. Governing equations

The principle of virtual work is utilised here to determine the governing equations; the variation of strain energy of the beam is calculated by

$$\delta U = \int_A \left[N_x \delta\varepsilon_x^0 + N_z \delta\varepsilon_z^0 + M_x^b \delta k_x^b + M_x^s \delta k_x^s + Q_{xz} \delta\gamma_{xz}^0 + S_{xz} \delta\gamma_{xz}^1 \right] dA = 0, \tag{3.10}$$

where A is the surface and stress resultants N, M, Q, and S are the force and moment components represented in the following forms:

$$\begin{aligned} \begin{Bmatrix} N_x \\ M_x^b \\ M_x^s \end{Bmatrix} &= \int_{-h/2}^{h/2} (\sigma_x) \begin{Bmatrix} 1 \\ z \\ f(z) \end{Bmatrix} dz, \qquad N_z = \int_{-h/2}^{h/2} \sigma_z g'(z)\, dz, \\ \begin{Bmatrix} S_{xz} \\ Q_{xz}^s \end{Bmatrix} &= \int_{-h/2}^{h/2} (\tau_{xz}) \begin{Bmatrix} \mathrm{g(z)} \\ f'(z) \end{Bmatrix} dz. \end{aligned} \tag{3.11}$$

The variation of potential energy of the applied mechanical loads can be expressed as

$$\delta V = -\int_A q\delta(w_0(x) + g(z)\theta(x))\,dA - \int_A N_0 \frac{d(w_0 + g(z)\theta(x))}{dx}\frac{d\delta(w_0 + g(z)\theta(x))}{dx}\,dA. \tag{3.12}$$

Substituting the expressions from Eqs. (3.10) and (3.12) of δU and δV, the variation of the potential energy of the beam can be expressed as:

$$\begin{aligned}\delta U - \delta V &= \int_A [N_x\delta\varepsilon_x^0 + N_z\delta\varepsilon_z^0 + M_x^b\delta k_x^b + M_x^s\delta k_x^s + Q_{xz}^\delta\gamma_{xz}^0 + S_{xz}^\delta\gamma_{xz}^1]\,dA \\ &\quad - \int_A q\delta w_0\,dA - \int_A qg(z)\delta\theta\,dA \\ &\quad - \int_A N_0\frac{d(w_0 + g(z)\theta(x))}{dx}\,\frac{d\delta(w_0 + g(z)\theta(x))}{dx}\,dA = 0.\end{aligned} \tag{3.13}$$

Integrating by parts and collecting the coefficients of δu_0, δv_0, δw_0, and $\delta\theta$, from Eqs. (3.7) into Eqs. (3.9), the following governing equations of the beam are obtained:

$$\begin{aligned}&\delta u_0: \ \frac{\partial N_x}{\partial x} = 0,\\ &\delta w_0: \ \frac{\partial^2 M_x^b}{\partial x^2} + q + N_0\frac{\partial^2 w}{\partial x^2} = 0,\\ &\delta\theta: \ -N_z - k_1 M_x^s + k_1 A'\frac{\partial Q_{xz}}{\partial x} + \frac{\partial S_{xz}}{\partial x} + qg(z) + N_0 g(z)^2\frac{\partial^2 w}{\partial x^2} = 0.\end{aligned} \tag{3.14}$$

Using Eqs. (3.7), (3.8) and (3.9b), the stress resultants are obtained as:

$$\begin{Bmatrix} N \\ M_x^b \\ M_x^s \end{Bmatrix} = \begin{bmatrix} A & B & B^s \\ B & D & D^s \\ B^s & D^s & H^s \end{bmatrix} \begin{Bmatrix} \varepsilon_x^0 \\ k_x^b \\ k_x^s \end{Bmatrix} + \begin{bmatrix} L \\ L^a \\ R \end{bmatrix} \varepsilon_0^z, \tag{3.15a}$$

$$\begin{Bmatrix} Q \\ S \end{Bmatrix} = \begin{bmatrix} F^s & X^s \\ X^s & A^s \end{bmatrix} \begin{Bmatrix} \gamma^0 \\ \gamma^1 \end{Bmatrix}, \qquad N_z = R^a\varepsilon_z^0 + L(\varepsilon_x^0) + L^a(k_x^b) + R(k_x^s), \tag{3.15b}$$

where

$$\{A \ B \ D \ B^s \ D^s \ H^s\} = \int_{-h/2}^{h/2} \lambda(z)[1,\ z,\ z^2,\ f(z),\ zf(z),\ f^2(z)] \begin{Bmatrix} \frac{1-\nu}{\nu} \\ 1 \\ \frac{1-2\nu}{2\nu} \end{Bmatrix} dz, \tag{3.15c}$$

$$\text{(3.15d)}\quad S=\{S_{xz}\},\quad Q=\{Q_{xz}\},\quad \begin{Bmatrix} L \\ L^a \\ R \\ R^a \end{Bmatrix} = \int_{-h/2}^{h/2} \lambda(z) \begin{Bmatrix} 1 \\ z \\ f(z) \\ g'(z)\frac{1-v}{v} \end{Bmatrix} g'(z)\,dz,$$

$$F^s = F^s_{44},\quad A^s = A^s_{44},\quad X^s = X^s_{44},$$

$$\text{(3.15e)}\qquad (F^s_{44}, X^s_{44}, A^s_{44}) = \int_{-h/2}^{h/2} \left(\frac{E(z)}{2(1+v)} [f'^2(z), f'(z)g(z), g^2(z)] \right) dz.$$

Substituting Eqs. (3.7), (3.15), (3.16) into Eqs. (3.14), the equilibrium equations are defined by:

$$\begin{aligned}
\delta u_0 :\ & A\frac{\partial^2 u_0}{\partial x^2} - B\frac{\partial^3 w_0}{\partial x^3} + (B^s k_1 + L)\frac{\partial \theta}{\partial x} = 0,\\
\delta w_0 :\ & B\frac{\partial^3 u_0}{\partial x^3} - D\frac{\partial^4 w_0}{\partial x^4} + (D^s_{11} k_1 + L^a)\frac{\partial^2 \theta}{\partial x^2} + q + N_0\frac{\partial^2 w}{\partial x^2} = 0,\\
\delta \theta :\ & -(L + k_1 B^s_{11})\frac{\partial u_0}{\partial x} + (L^a + k_1 D^s_{11})\frac{\partial^2 w_0}{\partial x^2} - (k_1^2 H^s_{11} + 2k_1 R + R^a)\theta\\
& + (k_1^2 A'^2 F^s_{44} + k_1 A' X^s_{44})\frac{\partial^2 \theta}{\partial x^2} + (A^s_{44} + k_1 A' X^s_{44})\frac{\partial^2 \theta}{\partial x^2}\\
& + qg(z) + N_0 g(z)^2 \frac{\partial^2 w}{\partial x^2} = 0.
\end{aligned} \tag{3.16}$$

The critical buckling load is determined using the stability equations, which are formulated based on the principle of virtual forces and the criteria of adjacent equilibrium state.

3.3. Exact solution for various boundary conditions of FG beam

The admissible functions in Table 1 can be used to construct the exact solution of Eqs. (3.17) for FGM beams under different boundary conditions [23],

$$\begin{Bmatrix} u_0(x,y) \\ w_0(x,y) \\ \theta(x,y) \end{Bmatrix} = \begin{Bmatrix} U_m & \frac{\partial X_m(x)}{\partial x} Y_n(x) \\ W_m & X_m(x) Y_n(x) \\ \theta_m & X_m(x) Y_n(x) \end{Bmatrix}, \tag{3.17}$$

where U_m, W_m, and θ_m are the unknown displacement coefficients.

TABLE 1. Admissible functions X_m, Y_n.

Boundary conditions	Admissible functions X_m and Y_n	
	X_m	Y_n
Simply-Supported (S-S)	$\sin(\alpha x)$	$\sin(\lambda x)$
Clamped-Clamped (C-C)	$\sin(\alpha x)\cos(\alpha x)$	$\sin(\lambda x)\sin(\lambda x)$
Clamped-Free (C-F)	$\cos^2(\alpha x)(\sin^2(\alpha x)+1)$	$\sin^2(\lambda x)$

By replacing the extensions of U_m, W_m and θ_m of Eqs. (3.16) in the equations of equilibrium (3.15), the analytical solutions can be obtained from

$$\begin{bmatrix} a_{11} & a_{12} & a_{13} \\ a_{12} & a_{22}+N_{cr} & a_{23} \\ a_{13} & a_{23} & a_{33} \end{bmatrix} \begin{Bmatrix} U_{mn} \\ W_{mn} \\ \theta_{mn} \end{Bmatrix} = \begin{Bmatrix} 0 \\ 0 \\ 0 \end{Bmatrix}, \tag{3.18}$$

in which:

$$\begin{aligned} a_{11} &= A_{11}L_{12}, & a_{21} &= -BL_{13}, \\ a_{12} &= -BL_{12}, & a_{22} &= DL_{13}, \\ a_{13} &= B^s k_1 L_{12} - LL_{12}, & a_{31} &= B^s k_1 L_{13} - LL_{13}, \\ a_{23} &= -D^s k_1 L_{13} + L_a L_{13}, & a_{32} &= -D^s k_1 L_{13} + L_a L_{13}, \\ a_{33} &= H_{11}^s k_1^2 L_9 - 2k_1 R L_{13} + R + A^2 F_{44}^s k_1^2 L_{13} - 2AX_{44}^s k L_{13} + A_{44}^s L_{13}, \end{aligned} \tag{3.19}$$

with

$$N_{cr} = N_0 L_9 \tag{3.20}$$

and

$$\begin{aligned} (\alpha_1) &= \int_0^b \int_0^l (X_m Y_m) X_m Y_m \, dx \, dy, \\ (\alpha_6, \alpha_{12}) &= \int_0^b \int_0^l (X_m' Y_m, X_m''' Y_m) X_m' Y_m \, dx \, dy, \quad b = 1, \\ (\alpha_9, \alpha_{11}, \alpha_{13}) &= \int_0^b \int_0^l (X_m'' Y_m, X_m'' Y_m'', X_m'''' Y_m) X_m Y_m \, dx \, dy. \end{aligned} \tag{3.21}$$

The transverse load $q(x)$ is also expanded in the Fourier series as

$$q = \sum_{m=1}^{\infty} q_m \sin \frac{m\pi x}{l}. \tag{3.22}$$

The Fourier coefficient (q_m) for sinusoidal and uniform loads are as follows:

$$q = \begin{cases} q_0 & \text{sinusoidal load } (m=1), \\ \dfrac{4q_0}{m\pi} & \text{uniform load } (m = 1, 3, 5, \ldots, \infty). \end{cases} \tag{3.23}$$

For the bending problem, put $N_0 = 0$, and for the buckling problem, put $q = 0$.

- Bending analysis

$$[K]\{\Delta\} = \{f\}. \tag{3.24}$$

- Buckling analysis

$$\{[K] - N_0[N]\}\{\Delta\} = \{0\}, \tag{3.25}$$

where $[K]$ is the stiffness matrix, $[N]$ is the geometric matrix due to the axial forces, $\{f\}$ is the force vector, $\{\Delta\}$ is the vector of unknowns, and N_0 is the axial force.

4. Numerical results and discussion

4.1. Convergence and validation study

In this paper, many numerical examples are provided and discussed to verify the accuracy of the quasi-3D shear deformation theory used to analyse the static bending and buckling of the FGM beam for various boundary conditions.

The properties of the materials used are:

- Ceramic (P_c: Alumina, Al_2O_3): $E_c = 380$ GPa; $\upsilon_c = 0.3$.
- Metal (P_m: Aluminum, Al): $E_m = 70$ GPa; $\upsilon_m = 0.3$.

The material properties of the FG beam vary continuously in the thickness direction according to the power law (P-FGM).

For simplicity, displacements, stresses and critical buckling loads are presented in the non-dimensional form:

$$\begin{aligned}
\bar{w} &= \frac{100E_m h^3}{q_0 l^4} w\left(x = \frac{l}{2}, z = 0\right), \\
\bar{u} &= \frac{100E_m h^3}{q_0 l^4} u\left(x = 0, z = -\frac{h}{2}\right), \\
\bar{\sigma}_{xx}(z) &= \frac{h}{q_0 l}\sigma_x\left(x = \frac{l}{2}, z = \frac{h}{2}\right), \quad \bar{\tau}_{xz}(z) = \frac{h}{q_0 l}\tau_{xz}\left(x = 0, z = 0\right), \\
N_{cr} &= N_0 \frac{12l^2}{E_m h^3}.
\end{aligned} \tag{4.1}$$

Table 2 presents the maximum nondimensionalised displacements and stresses of the beam for various power law index values and a length-to-thickness (l/h)

TABLE 2. Non-dimensional displacements and stresses of functionally graded beams ($l = 5h$).

k	Theory	Model	Sinusoidal load				Uniform load			
			$\bar{u}$	$\bar{w}$	$\bar{\sigma}_x$	$\bar{\tau}_{zx}$	$\bar{u}$	$\bar{w}$	$\bar{\sigma}_x$	$\bar{\tau}_{zx}$
0 ceramic	Present 2D	HSDT	0.7251	2.5019	3.0916	0.4768	0.9398	3.1653	3.8020	0.7333
	Present 3D	HSDT	0.7033	2.2829	2.7730	0.4291	0.9080	2.8951	3.4120	0.6599
	SAYYAD [26]	RSDT	0.7266	2.5004	3.0979	0.5072	0.9420	3.1635	3.8084	0.7764
	REDDY [27]	HSDT	0.7251	2.5020	3.0916	0.4769	0.9397	3.1654	3.8028	0.7305
	TIMOSHENKO [28]	FSDT	0.7129	2.5023	3.0396	0.3183	0.9210	3.1057	3.7501	0.4922
	BERNOULLI–EULER [29]	CBT	0.7129	2.2693	3.0396	–	0.9210	2.8783	3.7501	–
1	Present 2D	HSDT	1.7795	4.9457	4.7856	0.5241	2.3037	6.2594	5.8832	0.8011
	Present 3D	HSDT	1.6925	4.5110	4.2472	0.5122	2.1856	5.7207	5.2250	0.7579
	SAYYAD [26]	RSDT	1.7819	4.9432	4.7964	0.543	2.3074	6.2563	5.8957	0.8288
	REDDY [27]	HSDT	1.7793	4.9458	4.7856	0.5243	2.3037	6.2594	5.8850	0.8031
	TIMOSHENKO [28]	FSDT	1.7588	4.6979	4.6979	0.5376	2.2722	6.1790	5.7960	0.8313
	BERNOULLI–EULER [29]	CBT	1.7588	4.6979	4.6979	–	2.2722	5.7746	5.7960	–
2	Present 2D	HSDT	2.4048	6.3754	5.6002	0.4368	3.1130	8.0677	6.8820	0.8201
	Present 3D	HSDT	2.2725	5.7379	4.9624	0.4269	2.9344	7.2765	6.1056	0.7760
	SAYYAD [26]	RSDT	1.7819	4.9432	4.7964	0.543	3.1174	8.0666	6.8971	0.8485
	REDDY [27]	HSDT	2.4048	6.3754	5.6004	0.5521	3.1128	8.0677	6.8842	0.8446
	TIMOSHENKO [28]	FSDT	2.3794	6.2601	5.4356	0.6978	3.0739	7.9253	6.7678	1.0791
	BERNOULLI–EULER [29]	CBT	2.3794	5.8346	5.4856	–	3.0739	7.4003	6.7678	–
5	Present 2D	HSDT	2.8643	7.7722	6.6054	0.3856	3.7101	9.8280	8.1100	0.7398
	Present 3D	HSDT	2.7024	6.8041	5.7982	0.3768	3.4893	8.6286	7.1326	0.7000
	SAYYAD [26]	RSDT	2.4078	6.3745	5.6149	0.5553	3.7179	9.8414	8.1331	0.7654
	REDDY [27]	HSDT	2.8644	7.7723	6.6057	0.5314	3.7098	9.8281	8.1127	0.8114
	TIMOSHENKO [28]	FSDT	2.8250	7.5056	6.4382	0.9942	3.6496	9.4987	7.9430	1.5373
	BERNOULLI–EULER [29]	CBT	2.8250	6.8994	6.4382	–	3.6496	8.7508	7.9430	–
10	Present 2D	HSDT	2.9990	8.6530	7.9078	0.4223	3.8861	10.938	9.7128	0.6715
	Present 3D	HSDT	2.8432	7.5315	6.9432	0.4127	3.6709	9.5508	8.5406	0.6353
	SAYYAD [26]	RSDT	3.0054	8.6547	7.93	0.456	3.9858	10.94	9.7345	0.6947
	REDDY [27]	HSDT	2.9989	8.6530	7.9080	0.4224	3.8861	10.938	9.7141	0.6448
	TIMOSHENKO [28]	FSDT	2.9488	8.3259	7.7189	1.232	3.8096	10.534	9.5231	1.9050
	BERNOULLI–EULER [29]	CBT	2.9488	7.5746	7.7189	–	3.8096	9.6072	9.5231	–
∞ metal	Present 2D	HSDT	3.9363	13.582	3.0916	0.4768	5.1018	17.183	3.8020	0.7482
	Present 3D	HSDT	3.8178	12.393	2.7730	0.4660	4,9290	15.716	3.4120	0.7079
	SAYYAD [26]	RSDT	3.9444	13.574	3.098	0.5072	5.1133	17.173	3.8084	0.7741
	REDDY [27]	HSDT	3.9363	13.582	3.0916	0.4769	5.1021	17.183	3.8028	0.7305
	TIMOSHENKO [28]	FSDT	3.8702	12.552	3.0396	0.3183	5.0000	15.912	3.7501	0.4922
	BERNOULLI–EULER [29]	CBT	3.8702	12.319	3.0396	–	5.0000	15.625	3.7501	–

ratio of 5. To facilitate comparison, we specifically generated numerical results for a supported FG beam using different theories: RSDT proposed by Sayyad [26], HSDT by Reddy [27], FSDT by Timoshenko [28], and CBT [29]. It is observed from Table 2 that the transverse displacement reaches its maximum value when $k = \infty$, while it is minimised when $k = 0$. This behaviour is attributed to the increased flexibility of FG beams with higher power-law indices.

The second validation exercise scrutinised the validity of the current theoretical model by evaluating the buckling behaviour of a supported, functionally graded higher-order beam under the axial force (N_0). The study presents numerical data for the non-dimensional critical buckling load (N_{cr}) in Table 3, reflecting various power law indices and l/h ratios of 5 and 10. The findings demonstrate a high degree of concordance with the results reported by Sayyad *et al.* [26], Li and Batra [30], Nguyen *et al.* [31], and Vo *et al.* [32]. An analysis of Table 3 reveals that an increase in the power law index (k) corresponds to a reduction in the critical buckling load. Additionally, it is noted that the non-dimensional critical buckling load is greater for slender, thin beams and lesser for thicker beams. In contrast, the dimensional critical buckling load exhibits the opposite trend, being higher for thicker beams and lower for thinner beams.

Table 3. Non-dimensional critical buckling load (N_{cr}) of simply supported functionally graded beams.

l/h	Theory	Power law index (p)					
		0 (ceramic)	1	2	5	10	∞ (metal)
5	Present 2D	48.5957	24.5837	19.0709	15.6436	14.0512	8.95187
	Present 3D	49.6392	25.3720	19.8365	16.4111	14.6969	9.14404
	Sayyad [26]	48.6260	24.5966	19.0738	15.6220	14.0485	8.95730
	Li and Batra [30]	48.8350	24.6870	19.2450	16.0240	14.4270	–
	Nguyen *et al.* [31]	48.8350	24.6870	19.2450	16.0240	14.4270	–
	Vo *et al.* [32]	48.8372	24.6898	19.2479	16.0263	14.4286	–
	Vo *et al.* [32]	48.8401	24.6911	19.1605	15.7400	14.1468	–
10	Present 2D	52.2377	26.1408	20.3663	17.0818	15.4993	9.62275
	Present 3D	52.5388	26.6412	20.9111	17.5600	15.8360	9.67820
	Sayyad [26]	52.2463	26.1443	20.3669	17.0750	15.4982	9.62420
	Li and Batra [30]	52.3090	26.1710	20.4160	17.1920	15.6120	–
	Nguyen *et al.* [31]	52.3090	26.1710	20.4160	17.1940	15.6120	–
	Vo *et al.* [32]	52.3085	26.1728	20.4187	17.1959	15.6134	–
	Vo *et al.* [32]	52.3082	26.1727	20.3936	17.1118	15.5291	–

Table 4 serves as a validation of the current theory's efficacy in the buckling analysis of P-FGM beams under various boundary conditions, including Simply-Supported (S-S), Clamped-Clamped (C-C), and Clamped-Free (C-F).

The non-dimensional critical buckling load (N_{cr}) for P-FGM beams across these conditions has been compared. The normalised buckling loads calculated using this theory have been evaluated against the results published by KAHYA and TURAN [33], NGUYEN *et al.* [31]. The analysis of Table 4 indicates that the findings from this theory align closely with those from other theories. It is observed that the clamped (C-C) beams demonstrate the highest buckling loads, in contrast to the cantilever (C-F) beams, which show the lowest. Additionally, an increase in the power law index is associated with a decrease in normalised buckling loads, confirming the current theory's capability to accurately determine the critical buckling loads of P-FGM beams under varying boundary conditions.

TABLE 4. Comparison of the normalised buckling loads of functionally graded beams with different boundary conditions ($l/h = 5$).

Boundary conditions	Theory	k					
			1	2	5	10	∞
S-S	Present 2D	48.5957	24.5837	19.0709	15.6436	14.0512	8.95187
	Present 3D	49.6392	25.372	19.8365	16.4111	14.6969	9.14408
	SAYYAD [26]	48.626	24.5966	19.0738	16.622	14.0485	8.95730
	KAHYA and TURAN [33]	48.5907	24.5815	19.1617	15.9417	14.3445	8.95100
	NGUYEN *et al.* [31]	48.8406	24.6894	19.1577	15.7355	14.1448	–
C-C	Present 2D	152.148	79.4832	60.8785	46.8871	40.9883	28.0272
	Present 3D	171.629	89.382	69.6172	55.9988	49.4489	31.6159
	SAYYAD [26]	154.484	79.739	61.9488	49.5646	42.7493	27.9160
	KAHYA and TURAN [33]	151.943	79.3903	61.7449	49.5828	43.5014	27.9890
	NGUYEN *et al.* [31]	154.561	80.5940	61.7666	47.7174	41.7885	–
C-F	Present 2D	13.0542	6.5362	5.0958	4.2906	3.8527	2.3807
	Present 3D	14.2703	6.8319	5.2547	4.4028	3.9351	2.3945
	SAYYAD [26]	13.0719	6.557	5.0986	4.2931	3.8512	2.3819
	KAHYA and TURAN [33]	13.0594	6.5352	5.0981	4.2926	3.897	2.4057
	NGUYEN *et al.* [31]	13.0771	6.5427	5.0977	4.2772	3.882	–

4.2. Parametric study and discussions – porosity effect

Table 5 is related to the effect of porosity, various porosity patterns and both the HSDT theory 2D and quasi-3D on the displacement, axial and tangential stresses of the FGM beam under uniform and sinusoidal loads of the supported FGM porous beam. It is clear that the augmentation of the imperfection parameter Ω leads to a reduction in rigidity of the FGM beam, therefore increasing the dimensionless displacement and axial and tangential stresses of the FGM beam for both the HSDT theory 2D and quasi-3D.

TABLE 5. Effect of porosity coefficient on displacement, axial and tangential stresses of the FGM beam under uniform and sinusoidal loads ($k = 2$, $l/h = 5$).

Ω	Porosity	Theory	Sinusoidal load				Uniform load			
			$\bar{u}$	$\bar{w}$	$\bar{\sigma}_x$	$\bar{\tau}_{zx}$	$\bar{u}$	$\bar{w}$	$\bar{\sigma}_x$	$\bar{\tau}_{zx}$
0.1	Imperfect I	2D	4.0117	10.0092	7.5654	0.65966	3.1000	7.90842	6.1578	0.42978
		3D	3.7664	9.01997	6.7400	0.59434	2.9168	7.11256	5.4770	0.45683
	Imperfect II	2D	3.3627	8.60362	7.1118	0.62666	2.5978	6.79941	5.7872	0.40840
		3D	3.1638	7.72134	6.3028	0.57909	2.4501	6.08864	5.1234	0.42814
	Imperfect III	2D	3.2747	8.51557	6.8494	0.66616	2.5298	6.72963	5.5728	0.43398
		3D	3.0878	7.67235	6.0708	0.61833	2.3912	6.05000	4.9350	0.45383
	Imperfect IV	2D	3.6552	9.26416	7.2652	0.70298	2.8242	7.31949	5.9102	0.45776
		3D	3.4390	8.38694	6.4682	0.64585	2.6630	6.61344	5.2574	0.48142
0.2	Imperfect I	2D	5.7165	13.5423	8.8018	0.64338	4.4190	10.6970	7.1596	0.41928
		3D	5.3374	12.2015	7.9040	0.52656	4.1333	9.62117	6.4234	0.46753
	Imperfect II	2D	3.6675	9.24922	7.3616	0.57274	2.8338	7.31014	5.9938	0.37352
		3D	3.4438	8.25355	6.5216	0.52000	2.6669	6.50830	5.3008	0.39541
	Imperfect III	2D	3.4542	9.01722	6.8112	0.661	2.6685	7.12642	5.5434	0.43068
		3D	3.2579	8.11411	6.0346	0.60717	2.5232	6.39835	4.9044	0.45303
	Imperfect IV	2D	4.4286	10.9440	7.8216	0.7388	3.4227	8.64475	6.3612	0.48090
		3D	4.1562	9.94443	7.0002	0.65798	3.2186	7.84152	5.6896	0.51429
0.3	Imperfect I	2D	10.293	22.6130	11.947	0.61458	7.9611	17.8528	9.7118	0.40056
		3D	9.5378	20.4186	10.963	0.30961	7.3837	16.1000	8.9024	0.52590
	Imperfect II	2D	4.0504	10.0478	7.6456	0.50518	3.1298	7.94198	6.2262	0.32970
		3D	3.7947	8.90770	6.7690	0.44731	2.9389	7.02406	5.5018	0.35374
	Imperfect III	2D	3.6547	9.58325	6.7718	0.65494	2.8232	7.57418	5.5106	0.42680
		3D	3.4480	8.61043	5.9928	0.59388	2.6706	6.78976	4.8722	0.45216
	Imperfect IV	2D	5.6230	13.4964	8.6956	0.779	4.3469	10.6580	7.0694	0.50682
		3D	5.2595	12.3059	7.8458	0.65383	4.0725	9.70347	6.3744	0.55838

The influence of porosities distribution on critical buckling load N_{cr} of FG beams for volume fraction index = 2 for the HSDT theory 2D and quasi-3D is depicted in Table 6. The porosity coefficient is chosen as Ω egal (0.1 to 0.4). It is clear that the buckling load obtained for imperfect beams ($\Omega = 0.1$) is bigger than the other values of the porosity coefficient for the four distributions of porosity calculated. The critical buckling loads decreased as the porosity parameters increased for functionally graded porous beams for both used HSDT theories. This is because the mechanical properties, such as Young's modulus, are affected by the porosity, leading to a decrease in the beam's ability to resist buckling loads.

Table 7 shows buckling loads N_{cr} of various imperfections of FG porous beams with various boundary conditions for volume fraction index $k = 2$ for

TABLE 6. Effect of porosity coefficient on non-dimensional critical buckling load of FG beams ($k = 2$).

l/h	Porosity	Theory	Porosity coefficient $*10^3$					
			0.1	0.15	0.2	0.25	0.3	0.4
5	Imperfect I	2D	15.3742	13.4197	11.3663	9.18052	6.81048	1.10708
		3D	16.0732	14.0783	11.9754	9.72548	7.26625	1.20860
	Imperfect II	2D	17.8817	17.2655	16.6325	15.9810	15.3092	13.8941
		3D	18.6576	18.0480	17.4233	16.7810	16.1196	14.7278
	Imperfect III	2D	18.0672	17.5645	17.0612	16.5572	16.0526	15.0407
		3D	18.7908	18.2675	17.7433	17.2189	16.6940	15.6421
	Imperfect IV	2D	16.6112	15.3500	14.0646	12.7518	11.4079	8.60828
		3D	17.3099	16.0158	14.6975	13.3510	11.9720	9.09205
20	Imperfect I	2D	16.6054	14.4320	12.1534	9.73844	7.14343	1.11343
		3D	17.1002	14.9279	12.6413	10.2025	7.55479	1.21450
	Imperfect II	2D	19.4767	18.8317	18.1680	17.4839	16.7762	15.2797
		3D	19.9735	19.3375	18.6827	18.0072	17.3083	15.8275
	Imperfect III	2D	19.6585	19.1284	18.5976	18.0668	17.5355	16.4716
		3D	20.1037	19.5564	19.0085	18.4604	17.9120	16.8138
	Imperfect IV	2D	17.9131	16.4854	15.0385	13.5703	12.0782	9.00925
		3D	18.3936	16.9649	15.5149	14.0410	12.5392	9.43379

HSDT theory 2D and quasi-3D. The porosity coefficient is taken as Ω equal to (0.1 to 0.4). It is clear that the buckling load obtained for imperfect beams ($\Omega = 0.1$) is bigger than the other values of the porosity coefficient for the four distributions of porosity calculated. The values of buckling loads N_{cr} for the C-C boundary condition are more important than S-S, than C-F boundary condition because a clamped FG porous beam offers the greatest resistance to bending and rotation; this translates to a higher critical buckling load compared to supported or clamped-free ends, which allow for more movement and deflection.

A comparison study of the central deflection (w), the axial stress σ_{xz} and the transverse shear stress τ_{xz} are reported in Figs. 2–7 for P-FGM FG porous beams with various porous models and subjected to both sinusoidal and uniform distribution loads. Figures 2 and 7 indicate the effect of the side-to-thickness ratio l/h and the porosity models on the central deflections w (Fig. 2), and the dimensionless stress σ_{xx} (Fig. 7) of FG porous FG beams with volume fraction $k = 2$ and porosity coefficient Ω is chosen as 0.2. It is noted that for the various porous models of FG beams, the central deflections (w) decreases with increasing side-to-thickness ratio; this is because of the porosity coefficient's effect on the beam's stiffness; it is the opposite with the dimensionless stress σ_{xx}, which increases with increasing the side-to-thickness ratio, this is because the FG beam

Table 7. Buckling loads (N_{cr}) of various imperfect beams with various boundary conditions ($k = 1$, $l/h = 5$).

Boundary condition	Porosity	Theory	Porosity coefficient $*10^3$					
			0.1	0.15	0.2	0.25	0.3	0.4
S-S	Imperfect I	2D	21.2244	19.4999	17.7371	15.9280	14.0614	10.0904
		3D	21.9593	20.2072	18.4156	16.5758	14.6753	10.6179
	Imperfect II	2D	23.5620	23.0408	22.5124	21.9756	21.4301	20.3096
		3D	24.3473	23.8261	23.2981	22.7633	22.2208	21.1097
	Imperfect III	2D	23.5441	23.0225	22.4993	21.9745	21.4481	20.3896
		3D	24.2869	23.7425	23.1968	22.6493	22.1003	20.9963
	Imperfect IV	2D	22.2649	21.0900	19.9033	18.7044	17.4916	15.0200
		3D	23.0064	21.8092	20.6012	19.3811	18.1475	15.6329
C-C	Imperfect I	2D	69.1620	63.8644	58.4468	52.8780	47.1145	34.7272
		3D	77.7151	71.7265	65.6015	59.3071	52.7935	38.8061
	Imperfect II	2D	75.8357	73.9787	72.0973	70.1900	68.2547	64.2912
		3D	85.6060	83.6884	81.7492	79.7863	77.7985	73.7400
	Imperfect III	2D	76.0043	74.2585	72.5092	70.7551	68.9963	65.4617
		3D	85.4828	83.5265	81.5653	79.5991	77.6272	73.6649
	Imperfect IV	2D	72.8208	69.4080	65.9348	62.3945	58.7795	51.2923
		3D	81.5452	77.5597	73.5232	69.4289	65.2715	56.7300
C-F	Imperfect I	2D	5.7891	5.3457	4.8922	4.4261	3.9437	2.9068
		3D	5.9862	5.5003	5.0101	4.5129	4.0046	2.9306
	Imperfect II	2D	6.2958	6.1565	6.0154	5.8719	5.7262	5.4268
		3D	6.5651	6.4124	6.2582	6.1020	5.9438	5.6204
	Imperfect III	2D	6.3619	6.2157	6.0693	5.9225	5.7753	5.4794
		3D	6.6253	6.4616	6.2984	6.1355	5.9729	5.6485
	Imperfect IV	2D	5.9493	5.6354	5.3183	4.9979	4.6739	4.0134
		3D	6.1660	5.8180	5.4705	5.1233	4.7757	4.0773

is more susceptible to bending and can experience higher stresses at the same load due to its lower bending stiffness.

Figure 3 shows the variation of the non-dimensional central deflection w versus non-dimensional length x/l of perfect and imperfect for various porous models of FG beams with the volume fraction $k = 2$ and the porosity coefficient $\Omega = 0.2$. It can be seen that the central deflections w have maximum values at the central of the beam ($x = l/2$) significant differences between the results obtained by the porosity distribution models, where the uneven porosity distribution model (imperfect I) is higher than that for the other models.

Figure 4 demonstrates the variation of the non-dimensional central deflection w versus the porosity coefficient Ω of various porous models of FG beams

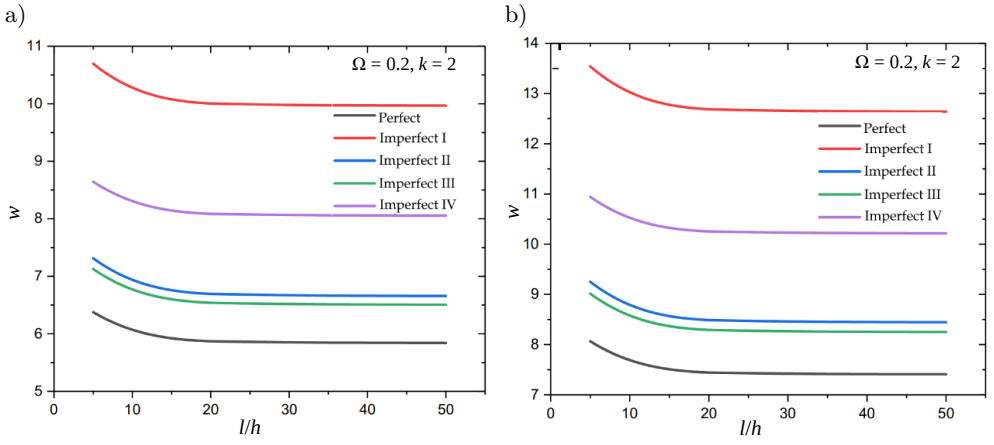

FIG. 2. Variation of the non-dimensional central deflection (w) versus the side-to-thickness ratio l/h of perfect and imperfect beams ($k = 2$); (a) subjected to sinusoidal distributed loads, (b) subjected to uniform distributed loads.

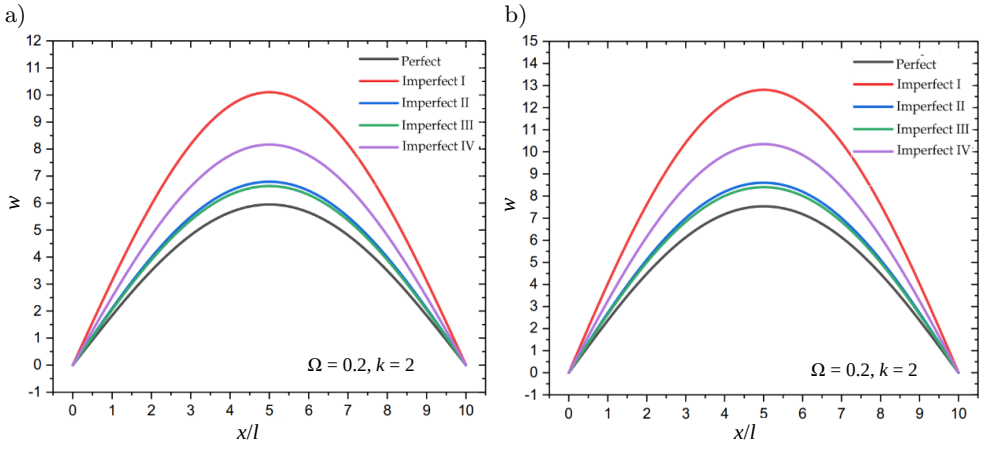

FIG. 3. Variation of the non-dimensional central deflection (w) versus non-dimensional length x/l of perfect and imperfect beams $l/h = 10$ ($k = 2$); (a) subjected to sinusoidal distributed loads, (b) subjected to uniform distributed loads.

with volume fraction $k = 2$ and the side-to-thickness ratio $l/h = 10$. It is observed that for the various porous models of FG beams, the central deflections w increase with increasing porosity coefficient. This is because the voids in porous materials have an uneven distribution of density and strength. This inhomogeneity can make the material less predictable in its deflection behaviour under load, with a tendency for larger deflections than a solid, homogeneous material.

Variation of the transverse shear stress τ_{xz} and the axial stress σ_{xx} through-the-thickness FG beams for various porous models with volume fraction $k = 2$

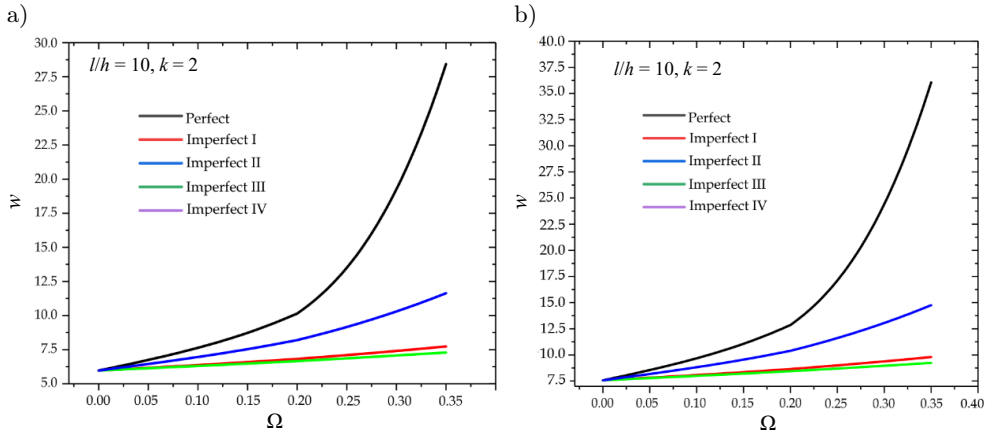

FIG. 4. Variation of the non-dimensional central deflection (w) versus porosity coefficient Ω of perfect and imperfect beams $l/h = 10$ ($k = 2$); (a) subjected to sinusoidal distributed loads, (b) subjected to uniform distributed loads.

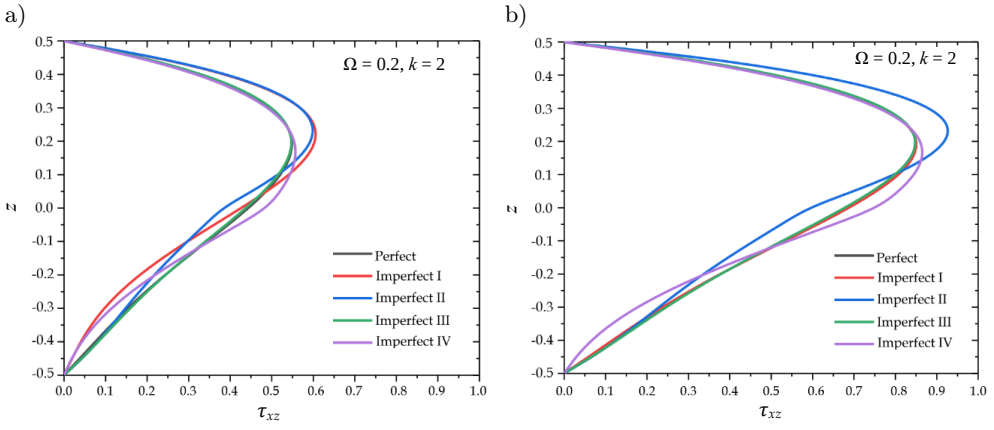

FIG. 5. The variation of the transverse shear stress τ_{xz} through-the-thickness of perfect and imperfect beams $l/h = 10$ ($k = 2$); (a) subjected to sinusoidal distributed loads, (b) subjected to uniform distributed loads.

and the side-to-thickness ratio $l/h = 10$ are shown in Figs. 5 and 6, respectively. Figure 5 illustrates our proposed theory, which predicts a parabolic distribution of transverse shear stress throughout the depth of FG porous beams. This theory also fulfils the crucial condition of zero shear stress at the top and bottom surfaces of the beams. Overall, it is noted that the present results show excellent agreement with higher-order theories. In addition, the magnitude of the tensile stresses given in Fig. 6 is greater than the magnitude of the compressive stresses in FG porous beams. Due to varying properties through the thickness, the axial stress for the FG porous beam is not zero at the neutral axis.

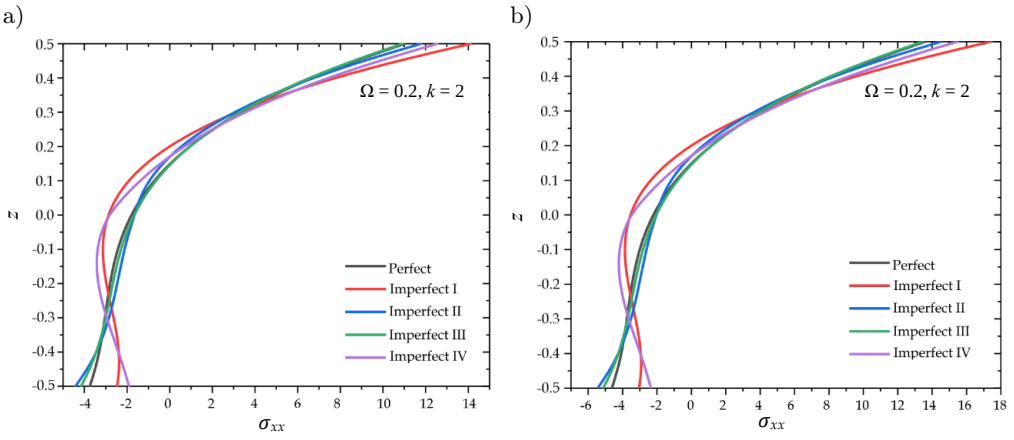

FIG. 6. The variation of the axial stress σ_{xx} through-the-thickness of perfect and imperfect beams $l/h = 10$ ($k = 2$); (a) subjected to sinusoidal distributed loads, (b) subjected to uniform distributed loads.

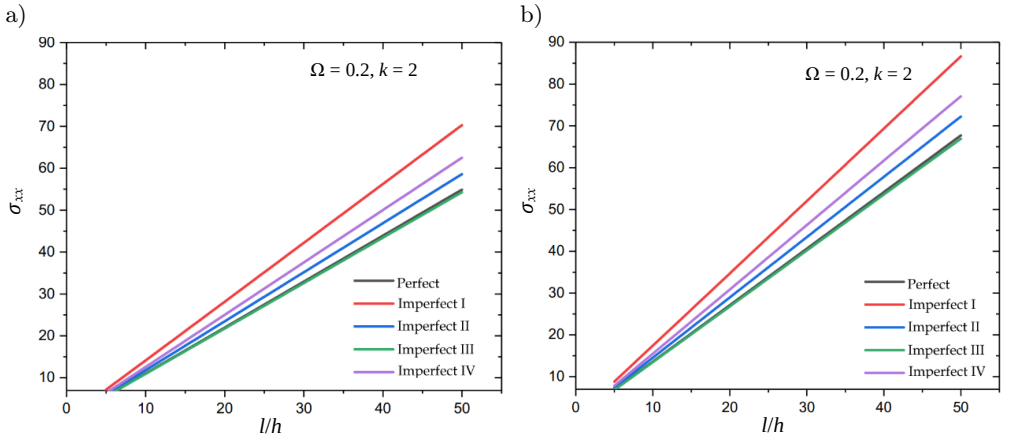

FIG. 7. The variation of the axial stress σ_{xx} versus the side-to-thickness ratio l/h of perfect and imperfect beams ($k = 2$); (a) subjected to sinusoidal distributed loads, (b) subjected to uniform distributed loads.

Variations of the non-dimensional critical buckling load of both boundary conditions simply supported (S-S) and clamped (C-C) of FG porous beams with respect to l/h ratios are shown in Fig. 8. It is clearly that the critical buckling load N_{cr} is almost constant after $l/h = 20$ for all porous models. Figure 9 shows the effect of the porosity coefficient on buckling loads N_{cr} of FG porous beams for both boundary conditions. It is noted that for the various porous models of FG beams, buckling loads, N_{cr} decreases with increasing porosity coefficient.

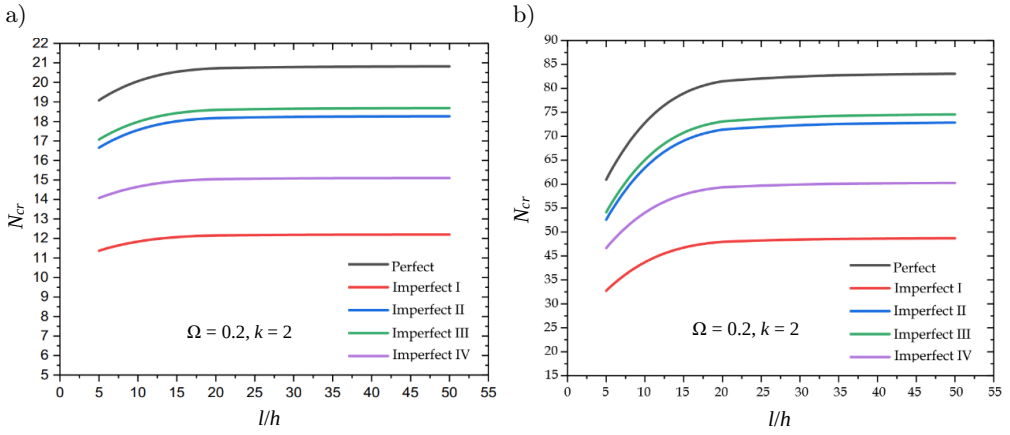

FIG. 8. The variation of buckling loads versus the side-to-thickness ratio l/h of perfect and imperfect beams ($k = 2$, $\Omega = 0.2$); (a) S-S boundary condition, (b) C-C boundary condition.

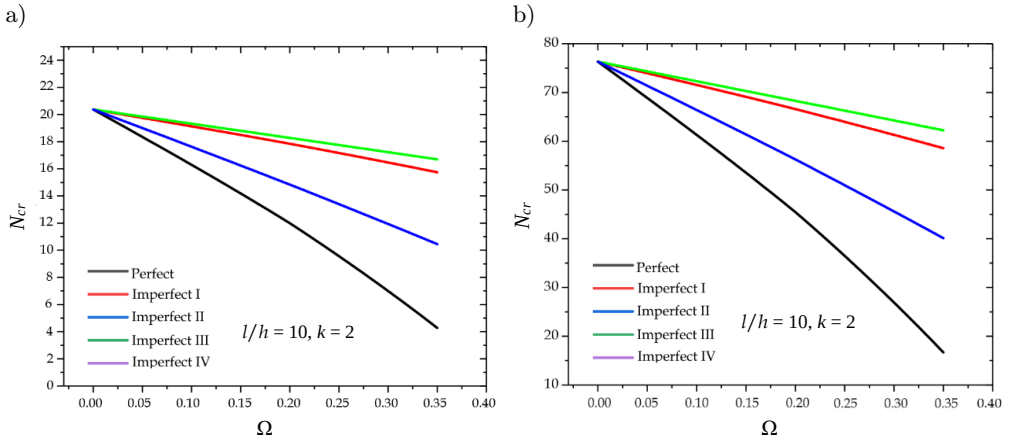

FIG. 9. Effect of porosity coefficient on buckling loads N_{cr} of FG porous beams ($k = 2$, $l/h = 10$); (a) S-S boundary condition, (b) C-C boundary condition.

It is noted that the values of clamped (C-C) boundary conditions are greater than supported (S-S) for Figs. 8 and 9.

5. Conclusions

This article presents a numerical study on the bending and buckling analysis of functionally graded beams using a simple integral shear deformation theory in 2D and quasi-3D. It introduces the coefficient n to transition from 2D to quasi-3D theories while maintaining continuity smoothly. This approach allows for analyzing the equilibrium and stability of FG beams. The proposed beam has four

types of porous distribution and is investigated under static bending and buckling with varied boundary conditions according to power law P-FGM distributions. This theory reduces the number of unknowns and governing equations while integrating the effects of thickness stretching into integral terms. The governing equations are attained from the static version of the principle of virtual work, and analytical solutions for various boundary conditions for porous and perfect beams are reached by deriving governing equations. Multiple validation examples are presented, and the current quasi-3D theory's numerical results accurately predict different FG porous beams' bending and buckling responses. From the results obtained and the parametric study, several conclusions can be reached:

- For various porous models of FG beams, the central deflection (w) decreases as the side-to-thickness ratio increases, reaching its maximum value for a perfect beam.
- The dimensionless stress σ_{xx} increases with a higher side-to-thickness ratio because the FG beam becomes more prone to bending, leading to greater stresses under the same load due to its reduced bending stiffness.
- The central deflections (w) reach their maximum values at the centre of the beam ($x = l/2$), with significant differences observed between the results of the porosity distribution models. The uneven porosity distribution model (Imperfect I) yields higher deflections compared to the other models.
- For different porous models of FG beams, the central deflection (w) increases as the porosity coefficient rises.
- The tensile stresses shown in Fig. 6 have a greater magnitude than the compressive stresses in FG porous beams.
- The critical buckling load of the porous FGM beam increases with the increase in the side-to-thickness ratio.
- The critical buckling load of the porous FGM beam decreases with increasing porosity.
- The boundary conditions can significantly influence the stability of the porous FGM beam

This difference is primarily attributed to the presence of porosity, which significantly affects the behaviour of FG beams. As a result, porosity must be considered in the design process to accurately analyse the bending behaviour of FG beams, particularly for specialised applications in aerospace, automotive, and civil engineering.

References

1. D. Chen, K. Gao, J. Yang, L. Zhang, *Functionally graded porous structures: Analyses, performances, and applications – A review*, Thin-Walled Structures, **191**, 111046, 2023, https://doi.org/10.1016/j.tws.2023.111046.

2. E.K. Njim, M. Al-Waily, S.H. Bakhy, *A critical review of recent research of free vibration and stability of functionally graded materials of sandwich plate*, IOP Conference Series: Materials Science and Engineering, **1094**, 1, 012081, 2021, https://doi.org/10.1088/1757-899X/1094/1/012081.

3. M. Dhuria, N. Grover, K. Goyal, *Influence of porosity distribution on static and buckling responses of porous functionally graded plates*, Structures, **34**, 1458–1474, 2021, https://doi.org/10.1016/j.istruc.2021.08.050.

4. E. Reissner, Y. Stavsky, *Bending and stretching of certain types of heterogeneous aeolotropic elastic plates*, Journal of Applied Mechanics, **28**, 402–408, 1961, https://doi.org/10.1115/1.3641719.

5. E. Arshid, A.R. Khorshidvand, *Free vibration analysis of saturated porous FG circular plates integrated with piezoelectric actuators via differential quadrature method*, Thin-Walled Structures, **125**, 220–233, 2018, https://doi.org/10.1016/j.tws.2018.01.007.

6. L. Della Croce, P. Venini, *Finite elements for functionally graded Reissner–Mindlin plates*, Computer Methods in Applied Mechanics and Engineering, **193**, 9–11, 705–725, 2004, https://doi.org/10.1016/j.cma.2003.09.014.

7. S. Trabelsi, A. Frikha, S. Zghal, F. Dammak, *Thermal post-buckling analysis of functionally graded material structures using a modified FSDT*, International Journal of Mechanical Sciences, **144**, 74–89, 2018, https://doi.org/10.1016/j.ijmecsci.2018.05.033.

8. A. Tamrabet, C. Mourad, N. Ali Alselami, A. Menasria, B. Mamen, A. Bouhadra, *Efficient kinematic model for stability analysis of imperfect functionally graded sandwich plates with ceramic middle layer and varied boundary edges*, Journal of Computational Applied Mechanics, **55**, 2, 184–200, 2024, https://doi.org/10.22059/jcamech.2024.371464.947.

9. F.Y. Genao, J. Kim, K.K. Żur, *Nonlinear finite element analysis of temperature-dependent functionally graded porous micro-plates under thermal and mechanical loads*, Composite Structures, **256**, 112931, 2021, https://doi.org/10.1016/j.compstruct.2020.112931.

10. M.W. Zaitoun, A. Chikh, A. Tounsi, M.A. Al-Osta, A. Sharif, S.U. Al-Dulaijan, M.M. Al-Zahrani, *Influence of the visco-Pasternak foundation parameters on the buckling behavior of a sandwich functional graded ceramic–metal plate in a hygrothermal environment*, Thin-Walled Structures, **170**, 108549, 2022, https://doi.org/10.1016/j.tws.2021.108549.

11. E. Carrera, *Theories and finite elements for multilayered, anisotropic, composite plates and shells*, Archives of Computational Methods in Engineering, **9**, 87–140, 2002, https://doi.org/10.1007/BF02736649.

12. E. Carrera, G. Giunta, P. Nali, M. Petrolo, *Refined beam elements with arbitrary cross-section geometries*, Computers & Structures, **88**, 5–6, 283–293, 2010, https://doi.org/10.22059/jcamech.2024.371464.94710.1016/j.compstruc.2009.11.002.

13. M. AREFI, M. KIANI, A.M. ZENKOUR, *Size-dependent free vibration analysis of a three-layered exponentially graded nano-/micro-plate with piezomagnetic face sheets resting on Pasternak's foundation via MCST*, Journal of Sandwich Structures & Materials, **22**, 1, 55–86, 2020, https://doi.org/10.1177/1099636217734279.

14. W.-Y. JUNG, W.-T. PARK, S.-C. HAN, *Bending and vibration analysis of S-FGM microplates embedded in Pasternak elastic medium using the modified couple stress theory*, International Journal of Mechanical Sciences, **87**, 150–162, 2014, https://doi.org/10.1016/j.ijmecsci.2014.05.025.

15. A. SOLEIMANI, F. ZAMANI, H. HAGHSHENAS GORGANI, *Buckling analysis of three-dimensional functionally graded Euler–Bernoulli nanobeams based on the nonlocal strain gradient theory*, Journal of Computational Applied Mechanics, **53**, 1, 24–40, 2022, https://doi.org/10.22059/jcamech.2022.338327.689.

16. A. MENASRIA, A. TAMRABET, A. BOUHADRA, S. REFRAFI, N.A. ALSELAMI, B. MAMEN, A. TOUNSI, *Nonlinear temperature dependent and visco-elastic foundation effects on the free vibration of functionally graded sandwich plates with ceramic foam core*, The Journal of Strain Analysis for Engineering Design, **59**, 8, 542–558, 2024, https://doi.org/10.1177/03093247241273834.

17. N. HIMEUR, B. MAMEN, S. BENGUEDIAB, A. BOUHADRA, A. MENASRIA, B. BOUCHOUICHA, F. BOURADA, M. BENGUEDIAB, *Coupled effect of variable Winkler–Pasternak foundations on bending behavior of FG plates exposed to several types of loading,* Steel and Composite Structures, An International Journal, **44**, 3, 353–369, 2022, https://doi.org/10.12989/scs.2022.44.3.353.

18. H. BELARBI, B. BOUCHAM, F. BOURADA, A. KACI, M. BOURADA, A.J.P.M. TOUNSI, *Investigation on thermomechanical bending of functionally graded sandwich plates using a novel combined 2D integral plate model*, Physical Mesomechanics, **27**, 4, 472–484, 2024, https://doi.org/10.1134/S1029959924040118.

19. A. BERKIA, S. BENGUEDIAB, A. MENASRIA, A. BOUHADRA, F.B.B. MAMEN, A. TOUNSI, K.H. BENRAHOU, M. BENGUEDIAB, M. HUSSAIN, *Static buckling analysis of bi-directional functionally graded sandwich (BFGSW) beams with two different boundary conditions*, Steel and Composite Structures, **44**, 4, 503, 2022, https://doi.org/10.12989/scs.2022.44.4.503.

20. S. AL-HOURI, M.A. AL-OSTA, F. BOURADA, Q. GAWAH, A. TOUNSI, S. AL-DULAIJAN, *Analysis of porosity-dependent wave propagation in fg-cntrc beams utilizing an integral higher-order shear deformation theory*, International Journal of Structural Stability Dynamics, **25**, 1, 2550233, 2024, https://doi.org/10.1142/S0219455425502335.

21. M.H. GHAZWANI, A. ALNUJAIE, H. YOUZERA, S.A. MEFTAH, A. TOUNSI, *Nonlinear forced vibration investigation of the sandwich porous FGM beams with viscoelastic core layer*, Acta Mechanica, **235**, 2889–2904, 2024, https://doi.org/10.1007/s00707-024-03865-7.

22. R. SLIMANI, A. MENASRIA, M. ALI RACHEDI, C. MOURAD, S. REFRAFI, A.A. NIMER, A. BOUHADRA, B. MAMEN, *A novel quasi-3D refined HSDT for static bending analysis of porous functionally graded Plates*, Journal of Computational Applied Mechanics, **55**, 3, 519–537, 2024, https://doi.org/10.22059/jcamech.2024.372417.968.

23. A. TAMRABET, B. MAMEN, A. MENASRIA, A. BOUHADRA, A. TOUNSI, M.H. GHAZWANI, A. ALNUJAIE, S.R. MAHMOUD, *Buckling behaviors of FG porous sandwich plates*

with metallic foam cores resting on elastic foundation, Structural Engineering and Mechanics, **85**, 3, 289–304, 2023, https://doi.org/10.12989/sem.2023.85.3.289.

24. R. Patil, S. Joladarashi, R. Kadoli, *Effect of porosity and viscoelastic boundary conditions on FG sandwich beams in thermal environment: Buckling and vibration studies*, Structures, **56**, 105001, 2023, https://doi.org/10.1016/j.istruc.2023.105001.

25. P.V. Avhad, A.S. Sayyad, *On the static deformation of FG sandwich beams curved in elevation using a new higher order beam theory*, SĀDHANĀ Academy Proceedings in Engineering Sciences, **45**, 1, 188, 2020, https://doi.org/10.1007/s12046-020-01425-y.

26. A.S. Sayyad, Y.M. Ghugal, *Analytical solutions for bending, buckling, and vibration analyses of exponential functionally graded higher order beams*, Asian Journal of Civil Engineering, **19**, 607–623, 2018, https://doi.org/10.1007/s42107-018-0046-z.

27. S.P. Timoshenko, *On the correction for shear of the differential equation for transverse vibrations of prismatic bars*, The London, Edinburgh, and Dublin Philosophical Magazine and Journal of Science, **41**, 245, 744–746, 1921, https://doi.org/10.1080/14786442108636264.

28. J.N. Reddy, *A simple higher-order theory for laminated composite plates*, Journal of Applied Mechanics, **51**, 4, 745–752, 1984, https://doi.org/https://doi.org/10.1115/1.3167719.

29. J. Bernoulli, *Curvatura laminae elasticae*, Acta Eruditorum Lipsiae, **34**, 262–270, 1694.

30. S.-R. Li, R.C. Batra, *Relations between buckling loads of functionally graded Timoshenko and homogeneous Euler–Bernoulli beams*, Composite Structures, **95**, 5–9, 2013, https://doi.org/10.1016/j.compstruct.2012.07.027.

31. T.-K. Nguyen, T.P. Vo, H.-T. Thai, *Static and free vibration of axially loaded functionally graded beams based on the first-order shear deformation theory*, Composites Part B: Engineering, **55**, 147–157, 2013, https://doi.org/10.1016/j.compositesb.2013.06.011.

32. T.P. Vo, H.-T. Thai, T.-K. Nguyen, A. Maheri, J. Lee, *Finite element model for vibration and buckling of functionally graded sandwich beams based on a refined shear deformation theory*, Engineering Structures, **64**, 12–22, 2014, https://doi.org/10.1016/j.engstruct.2014.01.029.

33. V. Kahya, M. Turan, *Finite element model for vibration and buckling of functionally graded beams based on the first-order shear deformation theory*, Composites Part B: Engineering, **109**, 108–115, 2017, https://doi.org/10.1016/j.compositesb.2016.10.039.

Received November 28, 2024, revised version March 15, 2025.
Published online June 2, 2025.